The role of sulfur sinks and micro-structured supports on the performance of sulfur-sensitive non-PGM catalysts

The role of sulfur sinks and micro-structured supports on the performance of sulfur-sensitive non-PGM catalysts

Miguel García-Vázquez [a], Doga Satir [a], Juan M. González-Carballo [b], Philip Landon [b], Robert Tooze [b], Zhou Hong [c], Xuehong Gu [c], Guangru Zhang [c], Francisco R. García-García [a*]

[a]*School of Engineering, Institute for Materials and Processes, University of Edinburgh, Robert Stevenson Road, Edinburgh EH9 3FB, UK*

[b]*Drochaid Research Services, Purdie Building, North Haugh, St Andrews, Fife, KY16 9ST*

[c]*State Key Laboratory of Materials-Oriented Chemical Engineering, College of Chemical Engineering, Nanjing Tech University, 30 Puzhu Road(S), Nanjing 211816, P.R. China*

**Corresponding author: francisco.garcia-garcia@ed.ac.uk*

Abstract

The presence of traces of sulfur dioxide (i.e. 1-10 ppmV) alongside residual methane emissions induces the rapid deactivation of typical methane abatement catalysts. As a result, sulfur-induced poisoning is the main challenge faced by after-treatment technologies for residual methane abatement. The aim of this study was to synthesise a series of cobalt and molybdenum catalysts and assess their performance under realistic after-treatment conditions. The series of catalysts was characterised by BET, XRD, XPS, TPR, TGA under air flow, SEM, EDX and *in situ* DRIFTS. In addition, the performance of Co100 supported on an alumina hollow fibre was assessed under similar reaction conditions and characterised by SEM and EDX. It was found that the catalytic activity of the series of cobalt and molybdenum catalysts decreased in the following order: Co100 > Co80Mo20 > Co60Mo40. In addition, it was discovered that the other two catalysts (i.e. Co25Mo75 and Mo100) were inactive at 450°C due to the lack of highly active Co^{3+} species. Among the active catalysts, Co100 and Co80Mo20 experienced an initial activation followed by a gradual deactivation whereas Co60Mo40 experienced a 1 h interval with stable methane conversion levels in between the activation and deactivation. The delay in poisoning of the active cobalt (II,III) oxide phase of Co60Mo40 was attributed to the sulfur sink-properties of the cobalt molybdenum oxide present in this catalyst (i.e. 44 wt%). Finally, Co100 supported on an alumina hollow fibre achieved the highest methane conversion per unit mass of catalyst and its performance was stable for a duration of 2.5 h. The high activity was attributed to the large surface area provided by the geometry of the support while the higher resistance to sulfur poisoning was credited to the sulfur sink-properties of the alumina, which delayed the poisoning of the active phase.

Keywords

Residual methane oxidation, cobalt and molybdenum mixed oxide, hollow fibre, sulfur sink, natural gas

1. Introduction

The production of natural gas has been rising since the 1940s and it is forecasted that it will plateau around 2035 [1]. Natural gas is favoured as a bridge fuel since it is relatively abundant and releases up to 50% less carbon dioxide than coal and 20-30% less than oil [2]. Nevertheless, natural gas is mainly composed of methane, itself a greenhouse gas with a 20 year global warming potential of 84 [3]. The rise in methane consumption is going to result in an inevitable increase in residual methane emissions arising from the incomplete combustion of this gas [4]. Considering the electricity and transport sector, it is estimated that natural gas power plants and compressed natural gas-powered vehicles emit residual methane concentrations of up to 1500 ppmV [5,6]. In this respect, it can be concluded that the carbon dioxide emission reduction benefits of using natural are outweighed by the emission of non-combusted methane. In addition, the tightening emissions standards for the transport sector and the industry, which are shown in Fig.1, will give rise to the mandatory use of catalytic converters for residual methane abatement. Hence, targeting residual methane emissions will be a major factor contributing towards the real decarbonisation of our society during the gradual transition towards a 100%-renewable energy-powered future.

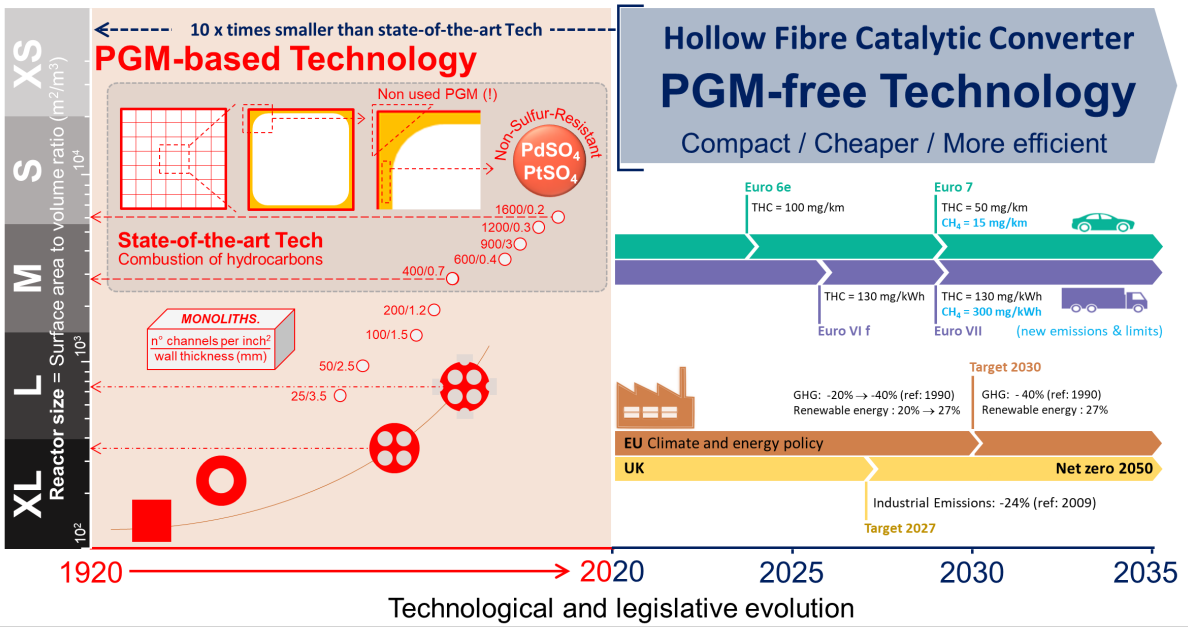

Fig. 1. Technological evolution of the catalytic industry and after-treatment technologies (left) and future emission standard legislations for the transport sector and the industry (right).

Among the different strategies that are available for the treatment of residual methane emissions, catalytic oxidation is the most favoured due to its environmental and economic advantages. There exists two types of catalysts for methane catalytic oxidation: i) noble metals [7–11] and ii) transition metal oxides [4,12–14].

Noble metal oxides have the highest activities for methane oxidation and their long use in the automotive industry has established them as the dominant oxidation catalysts in the market. Among these, palladium oxide is regarded as the most suitable for methane oxidation in air. However, this catalyst faces two major challenges: i) increasing prices due to the tightening of the legislation on traditional combustion engine vehicles (i.e. petrol and diesel cars) [15] and ii) the rapid deactivation of palladium oxide in the presence of traces of sulfur dioxide in the 1 to 100 ppmV range [11].

An alternative to noble metals are transition metal oxides, which have also been widely studied and can be subdivided into three groups: i) bulk transition metal oxides, ii) mixtures of transition metal oxides, and iii) mixed metal oxides. Among these, the last two groups are receiving more attention due to the potential synergistic effect arising from mixing two different metal oxides [4,12,16], which can lead to enhanced activities and higher resistance to sulfur poisoning. Even though this type of catalyst have a lower cost and competitive catalytic activity, the traces of sulfur dioxide present alongside residual methane emissions still remain a challenge due to sulfur dioxide-induced poisoning [13].

Both noble metal oxides and transition metal oxides share a common challenge: overcoming the sulfur dioxide-induced poisoning. Firstly, it is important to understand the source of the sulfur dioxide present alongside residual methane emissions. Sweet natural gas is odourless; therefore, 1 to 4 ppmV of sulfur odorants, which combust to give sulfur dioxide, are added for safety and legal reasons [17]. Additionally, sulfur dioxide can arise from the combustion of lubricant employed in compressed natural gas-powered engines [18]. Due to the inevitable presence of sulfur dioxide alongside residual methane emissions, three combinable approaches can be used to improve the efficacy of the catalysts: i) cyclical regeneration of the poisoned catalysts [7,8], ii) addition of sulfur sinks to slow down the rate at which catalysts get poisoned [10,19], and iii) design of sulfur-resistant catalysts [13,14].

The first approach, cyclical regeneration of the sulfur-poisoned catalysts, is the current state-of-the-art of noble metal-based catalyst technologies for residual methane abatement. Suvanto et al. [7,8] and

Gremminger et al. [9] have studied the poisoning mechanism of sulfur dioxide on palladium-based catalysts under different atmospheres, both through experimental work and simulations. In addition, these groups have proposed different in situ regeneration strategies. Gremminger et al. [9] achieved the regeneration through short pulses of fuel rich conditions at 500°C. Suvanto et al. [8] added steam to the reactant mixture. The hydrogen produced under these reaction conditions, via the steam reforming of methane and the water gas shift reaction, lead to the regeneration of the catalyst due to the low-temperature decomposition of the inactive palladium (II) sulfates.

The second approach, involving the presence of sulfur sinks, was discovered by Hoyos et al. [10] while studying the effects of hydrogen sulfide on a palladium catalyst supported on alumina and silica. Hoyos et al. observed that the deactivation of the catalyst was lower when supported on alumina than silica since it was found that alumina had the ability to store sulfate groups. Similarly, in our previous study [19] we have reported that the use of an alumina hollow fibre could not only improve the activity of a catalyst [20,21] but also act as a sulfur sink, increasing the lifetime of sulfur-sensitive catalysts. Finally, cobalt and molybdenum-based materials, which have typically been used as hydro-desulfurisation catalysts [22,23] due to their exceptional resitance to typical poisonous chemicals [24], have proven to be good sorbents for sulfur dioxide [25]. As a result, this type of materials have the potential to be used as sulfur sinks.

In addition, alumina hollow fibres are the ideal support for emission control due to their unprecedented S/V ratio and low pressure drop, which has two major advantages: i) the large surface area and internal geometry makes the impregnation of transition metal oxides competitive with palladium-based catalyst in terms of activity [19], and ii) the low pressure drop minimises backpressure, increasing fuel efficiency and thus reducing greenhouse gas emissions, overcoming the main limitation faced by traditional cordierite monoliths [26]. Fig. 1 shows that compared to the state-of-the-art PGM-based technology, the hollow fibre catalytic converter PGM-free technology allows for an after treatment technology which is 10 times smaller. Finally, alumina hollow fibre-based catalytic converters are easily scalable and have the potential to treat residual methane emissions arising from small household boilers to larger natural gas turbines [19].

The third approach, the design of sulfur-resistant catalysts, is closely linked to the thermodynamic equilibrium between the sulfur dioxide and the active phase of the catalyst. Ordóñez et al. [13] found that bulk chromium oxide is resistant to sulfur poisoning due to its low affinity towards sulfur dioxide. Nevertheless, in their study, in the absence of sulfur dioxide, the activity of bulk cobalt (II,III) oxide was 75% higher than that of bulk chromium oxide. Based upon this study, we [14] developed a bimetallic iron and chromium mixed oxide with activity levels superior to those of pure chromium oxide and a similar

resistance to sulfur poisoning. This study proved that the use of bimetallic catalysts has the potential to yield superior catalysts. The improved activity of the catalyst was attributed to the presence of a metastable iron and chromium-based spinel.

Cobalt (II,III) oxide has been widely studied and it has proven to be an attractive alternative to noble metal-based catalysts for residual methane oxidation at relatively low temperatures (i.e. 450 – 550°C) [4,13,27,28] following the Mars–Van Krevelen mechanism [29,30]. In addition, the exceptional resistance to typical poisonous chemicals of cobalt and molybdenum oxides [24] supports the study of bimetallic cobalt and molybdenum oxide as catalysts for the total oxidation of residual methane under realistic natural gas exhaust conditions. Finaly, the use of alumina hollow fibres have the potential to act as a sulfur sink while providing an ideal catalyst support for the development of catalytic converters.

The aim of the study presented herein is to synthesise a series of cobalt and molybdenum mixed oxides and assess their performance and sulfur resistance during the total oxidation of residual methane under realistic natural gas exhaust conditions (i.e. low temperature and presence of steam and sulfur dioxide). To the best of our knowledge this is the first study published in the literature were these catalysts are used for the total oxidation of methane. In addition, the best performing catalyst will be impregnated in an alumina hollow fibre and tested under the same reaction conditions in order to study the effect of this type of support on the performance and sulfur resistance of this catalyst. It is worth mentioning that this study has focused on the second and third approaches used to improve the efficacy of the catalysts under sulfur dioxide-containing atmospheres. Finally, several ex-situ and in-situ characterisation techniques have been used to gain a further understanding on the composition, morphology, redox properties and sulfur poisoning mechanism of the catalysts.

2. Experimental

2.1. Synthesis of the catalysts and hollow fibre supports

2.1.1. Synthesis of cobalt and molybdenum oxides

A series of cobalt and molybdenum mixed oxides were synthesised following the procedure described in the work of Halawy et al. [31]. Cobalt (II) nitrate and ammonium heptamolybdate were used as metal precursors. The procedure consisted on i) dissolving the cobalt (II) nitrate in distilled water, ii) adding the ammonium heptamolybdate, iii) drying the mixture in an oil bath set at 120°C under continuous stirring for approximately 2 h, and iv) calcining the resulting products in a static furnace (SNOL 3/1100 LHM01) under an air atmosphere at 500°C for a duration of 5 h using a heating ramp of 1°C/min.

The catalyst powders were pelletised by applying a load of 10 t in a 13 mm diameter cylinder for 5 min using a hydraulic press (AtlasTM Manual 15T Hydraulic Press). These pellets were then crushed and sieved to sizes ranging from 125 μm to 250 μm using stainless-steel sieves (Fieldmaster 78-800).The catalysts were labelled according to their cobalt:molybdenum molar ratio as follows: Co100, Co80Mo20, Co60Mo40, Co25Mo75 and Mo100.

2.1.2. Synthesis and impregnation of the hollow fibre support

Asymmetric 4-channel α-Al_2O_3 hollow fibre substrates were prepared using the phase inversion technique, followed by sintering at high temperatures. The detailed procedures for fabricating the substrates can be found elsewhere [32].

The impregnation of the 10 cm long micro-structured unit with Co100 precursor was carried out by pipetting the same solution used to synthesise the Co100 powder. The three step procedure was the following: i) impregnation of the micro-structured unit with the solution, ii) drying in a ventilated oven (SciQuip Oven-55S) at 100°C for 48 h, and iii) calcination under a 150 $mL \cdot min^{-1}$ air flow at 500°C for 3 h. The catalyst deposition was calculated by measuring the difference in weight of the micro-structured unit before and after impregnation.

2.2. Characterisation of the cobalt and molybdenum mixed oxides

2.2.1. Nitrogen Adsorption/Desorption Isotherms

The surface area of the fresh oxides and the reacted oxides were determined using nitrogen adsorption/desorption isotherms. The surface area of the oxides was measured after 1 h and 5 h of reaction. The samples were degassed under a vacuum at 250°C for 3 h before nitrogen adsorption/desorption measurements were taken at -196°C (Micrometrics Gemini VI Surface Area and Pore Size Analyzer)); 40 adsorption points and 40 desorption points were taken for each measurement. The Brunauer–Emmett–Teller (BET) method was used to calculate the specific surface area of the samples.

2.2.2. X-ray Powder Diffraction

X-ray diffraction (XRD) analysis was carried out to determine the crystal phase and crystallinity of each of the oxides here studied. A Panalytical X'Pert PRO Multipurpose Diffractometer was used to record powder x-ray diffraction (XRD) patterns using Co K(α) irradiation (λ=1.790307 Å), a step size of 0.02°, a

2θ range of 10°- 90° and a time step of 1.875°/min. The samples were placed in a silicon substrate zero-background sample holder. The obtained diffraction patterns have been analysed using X'Pert HighScore Plus software and compared to the ICDD database Powder Diffraction Files (PDF-3).

2.2.3. X-ray Photoelectron Spectroscopy of the cobalt and molybdenum mixed oxides

The surface chemical composition and surface element valence state of the oxides was studied using a Thermo ESCALAB 250 X-ray photoelectron spectrometer equipped with an Al-Ka X-ray source. The bond energies were referenced to the adventitious C 1s line (284.6 eV).

2.2.4. Temperature Programmed Reduction

Temperature programmed reduction (TPR) analysis was carried out in a Micromeritics Autochem II 2920 chemisorption analyser equipped with a TCD detector. A weight of 45 mg of oxide was used; these were dried prior to the experiment at 100°C for 1 h under a 30 ml/min argon flow. The TPR experiments were performed using a 50 ml/min flow of 10% hydrogen balanced in argon and a temperature ramp of 5°C/min from room temperature to 700°C. The profiles were deconvoluted using the "Origin version 2018b" peak-fitting software.

2.2.5. Thermogravimetric Analysis under air flow

Thermogravimetric analysis (TGA) under air flow was carried out using a METTLER TOLEDO thermogravimetric analyser. The 5 mg samples were heated up to 1000°C using a 10°C/min temperature ramp. A flowrate of 20 ml/min of air was flowed throughout the experiment.

2.2.6. Scanning Electron Microscopy and Energy Dispersive X-ray Spectroscopy of the cobalt and molybdenum mixed oxides

The surface topography of the oxides was studied using a Zeiss Crossbeam 550 Scanning Electron Microscope (SEM). The samples were uncoated, the working distance was set to 5.2 mm, and the FIB probe voltage and current were 30 kV and 50 pA, respectively. The elemental composition of the samples was studied by Energy-dispersive X-ray Spectroscopy (EDX) mapping using an Oxford Instruments X-Max 150 silicon drift detector, with an accelerating voltage of 15kV and a beam current of 500 pA. EDX maps were collected for approximately 3 minutes until signal to noise was sufficient.

2.3. Catalytic performance during the total oxidation of methane

2.3.1. Experimental Apparatus

The experimental apparatus used to carry out the total oxidation of methane reaction was equipped with: i) a packed bed reactor unit or the hollow fibre reactor unit shown in Fig. S1, ii) a reactor furnace (Elite Thermal Systems Limited. Model No: TSV12/32/150), iii) a network of electrical line heaters, iv) a water delivery system (IGI Systems), v) a gas delivery system and vi) a mass spectrometer (EcoSys-PTM Mass Spectrometer). Condensation within the lines was prevented by a network of electrical line heating tape and thermal insulating fabric, which kept the line temperatures above 160°C. The temperature of each of these lines was monitored using several k-type thermocouples distributed throughout the equipment.

The mass spectrometer (EcoSys-PTM Mass Spectrometer) is calibrated using synthetic air as a zero gas and the reaction mixture as a calibration gas. In addition, the ion current of synthetic air and that of the reaction mixture are used as references to calculate the range between 100% conversion and 0% conversion, respectively. Finally, experiments are reproducible (3 different runs) and have an error of ±1%.

Note that the hollow fibre reactor unit shown in Fig. S1 is the first of its kind. This homemade reactor allows for simple loading and unloading of the impregnated hollow fibres. In addition, the use of a graphite ferrule guaranteed a perfect seal, giving a higher accuracy for the mass spectrometry readings. Previously, hollow fibre reactor units have been sealed using epoxy resin and were single use. The features of our hollow fibre reactor unit make it possible to load smaller impregnated fibres while guaranteeing that the samples do not contain traces of epoxy, facilitating the characterisation of the impregnated hollow fibres after reaction.

The impregnated hollow fibre loaded into the hollow fibre reactor is a 4-channel asymmetric hollow fibre. The gas flows axially through the four channels of the fibre and diffuses radially through the finger regions of the fibre following Fick's laws of diffusion.

2.3.2. Experimental Procedure

The catalyst loading for the packed bed reactor experiments was of 500 mg; for the hollow fibre reactor experiments, it was calculated to be 53 mg. Similar reaction conditions were used for the packed bed reactor experiments and for the hollow fibre reactor experiment. The total oxidation of methane was performed at atmospheric pressure using a reactant flowrate of 150 ml/min and the following reactant

mixture: 312 ppmV of methane, 4.6 ppmV of sulfur dioxide, and 10%vol steam balanced in air. The gas mixture used in the reaction studies is custom made by BOC Ltd (UK). The certified concentrations of the tank are 347 ppmV of methane and 5.1 ppmV of sulfur dioxide balanced in air. Water is added using a water delivery system (IGI Systems) as indicated in section 2.3.1. The effluent gas was monitored by in-line mass spectrometry over a 5 h period. The conversion of methane, X(%), was calculated using eq. 1:

$$X(\%) = \frac{[CH_4]_{in} - [CH_4]_{out}}{[CH_4]_{in}} \times 100 \qquad \text{(eq. 1)}$$

It is worth mentioning that the likelihood of side reactions for the total oxidation of methane under the studied conditions is minimal, as the Gibbs free energy of the total oxidation of methane and its side reactions show in Fig. S2 indicates.

2.3.3. In situ Diffuse Reflectance Infrared Fourier Transform Spectroscopy

The surface morphology of the oxides under dry reaction conditions, 347 ppmV of methane and 5.1 ppmV of sulfur dioxide balanced in air (BOC, composition as stated), was analysed via *in situ* diffuse reflectance infrared fourier transform spectroscopy (DRIFTS) using a Shimadzu IR Tracer 100 spectrophotometer. A Harrick Praying Mantis high temperature reaction chamber was used to hold 25 mg of the powdered catalysts. During measurement, the reaction chamber was ramped at a rate of 10°C/min to 450°C under a 20 ml/min flowrate of nitrogen (BOC, 99.9%). Once the reaction chamber reached 450°C, the sample was activated for 30 min under air (BOC, 99.9%). Following this step, the air flow was switched to the dry reactant mixture consisting of 347 ppmV of methane and 5.1 ppmV of sulfur dioxide balanced in air (BOC, composition as stated) maintaining the flowrate at 20 ml/min for a duration of 5 h. Spectra were taken every 5 min throughout the 2 h experiment.

2.4. Characterisation of the impregnated hollow fibre

2.4.1. X-ray Photoelectron Spectroscopy of the hollow fibre-based reactor

The apparatus and experimental parameters used for XPS analysis of the hollow fibre-based reactor were similar to those described for the cobalt and molybdenum mixed oxides in section 2.2.3.

2.4.2. Scanning Electron Microscopy and Energy Dispersive X-ray Spectroscopy of the hollow fibre-based reactor

The apparatus and experimental parameters used for the SEM and EDX analysis of the hollow fibre-based reactor were similar to those described for the cobalt and molybdenum mixed oxides in section 2.2.6.

3. Results

3.1. Characterisation of the cobalt and molybdenum mixed oxides

3.1.1. Nitrogen Adsorption/Desorption Isotherms

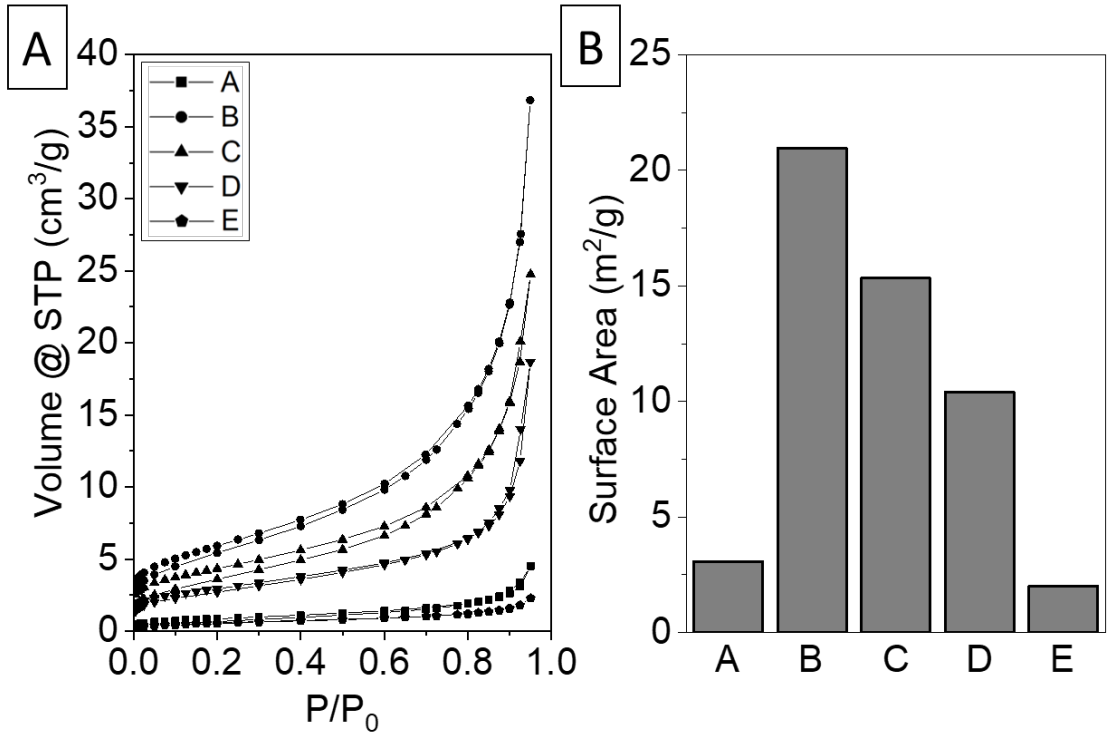

Fig. 2: A) Nitrogen adsorption and desorption isotherms of the fresh cobalt and molybdenum mixed oxides. Legend: Co100 (A-square), Co80Mo20 (B-circle), Co60Mo40 (C-triangle), Co25Mo75 (D-reversed triangle), and Mo100 (E-pentagon). B) Specific surface area of the fresh cobalt and molybdenum mixed oxides with increasing molybdenum content. From left to right: Co100 (A), Co80Mo20 (B), Co60Mo40 (C), Co25Mo75 (D) and Mo100 (E).

Nitrogen adsorption/desorption isotherms at −196°C corresponding to pure cobalt oxide, pure molybdenum oxide and cobalt and molybdenum mixed oxides are shown in Fig. 2A. According to the IUPAC classification, the cobalt and molybdenum mixed oxides show type IV nitrogen adsorption/desorption isotherms indicating that these are mesoporous materials. This is confirmed by the sharp increase in nitrogen adsorbed at high relative pressures ($0.5 < P/P_0 < 1$) corresponding to the filling of the mesopores. At high relative pressures, the cobalt and molybdenum mixed oxides' isotherms show a hysteresis loop that can be ascribed to type H3 according to the IUPAC classification. This indicates that the materials are composed of slit-shaped pores. This phenomenon is particularly noticeable for the cobalt-rich mixed oxides (i.e. Co80Mo20 and Co60Mo40). In the case of the pure oxides (i.e. Co100 and Mo100), the total volume of nitrogen adsorbed was so small that it was not possible to determine the type of isotherm obtained.

The Brunauer–Emmett–Teller (BET) surface areas of the different pure and mixed oxides here studied are plotted in Fig. 2B and tabulated in Table 1. Overall it can be observed that the surface area of the cobalt and molybdenum mixed oxides follows a volcano shape with a peak at 21 $m^2\ g^{-1}$ for Co80Mo20. Moreover, it can be seen that the surface area of the mixed oxides (i.e. 10-21 $m^2\ g^{-1}$) is larger than that of the pure oxides (i.e. 2-3 $m^2\ g^{-1}$).

Catalyst	**Co100**	**Co80Mo20**	**Co60Mo40**	**Co25Mo75**	**Mo100**
Fresh S_{BET} (m^2/g)	3±1	21±1	15±1	10±1	2±1
Reacted (1h) S_{BET} (m^2/g)	12±1	31±1	10±1	7±1	1±1
Reacted (5h) S_{BET} (m^2/g)	15±1	30±1	9±1	5±1	1±1

Table 1: Surface area of the cobalt and molybdenum oxides before (i.e. Fresh) and after 1 h and 5h reaction (i.e. reacted (1h) and reacted (5h)).

The surface area of the catalysts was affected by the reaction conditions. As can be seen in Table 1, the surface area of Co100 and Co80Mo20 increased whereas that of Co60Mo40, Co25Mo75 and Mo100 decreased after reaction.

3.1.2. X-ray Powder Diffraction

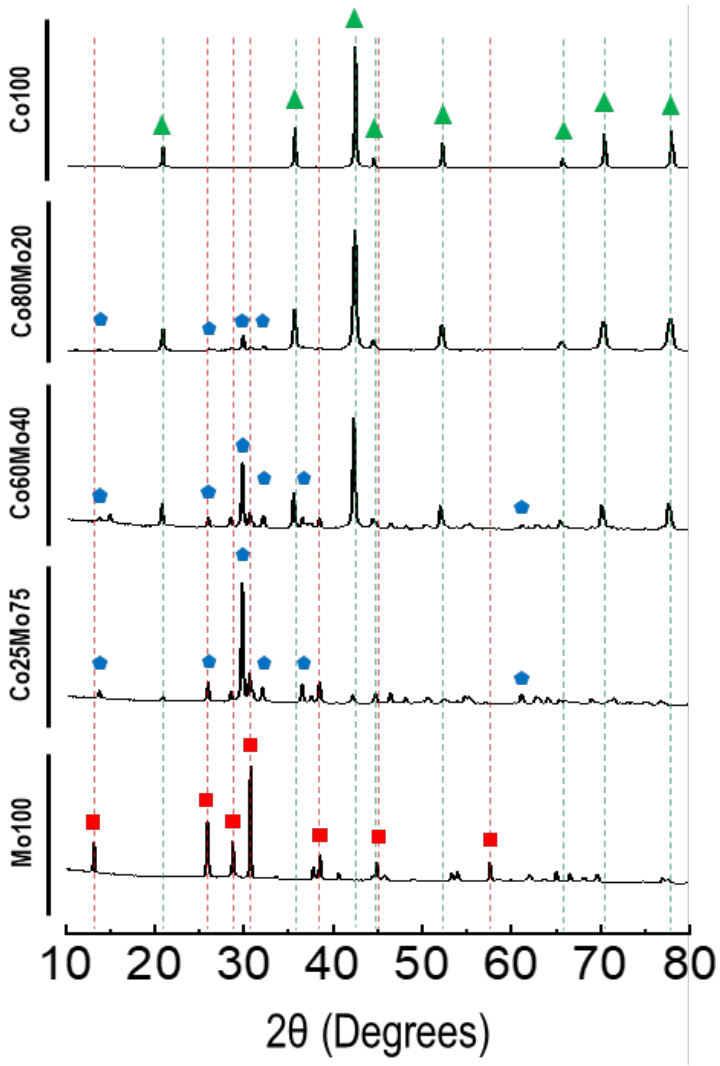

Fig. 3: XRD diffractogram of the fresh cobalt and molybdenum mixed oxides. Legend: cobalt (II,III) oxide, Co_3O_4, JCPDS 42-1467 (triangle-green); cobalt molybdenum oxide, $CoMoO_4$, JCPDS 21-0868 (pentagon-blue) and molybdenum trioxide, MoO_3, JCPDS 05-0508 (square-red).

X-ray Powder Diffraction (XRD) diffractograms of pure and mixed oxides studied herein are shown in Fig. 3. The XRD diffractograms of the fresh and aged samples are identical, as can be seen in Fig. S9. The sharp diffraction peaks observed indicate that all the oxides have a high degree of crystallinity. Note that, the XRD diffractograms of Co100, Mo100 and Co25Mo75 have been used as references to interpret the XRD diffractograms of the rest of the cobalt and molybdenum mixed oxides since the aforementioned

materials are composed of a single phase. In addition, the open literature and the Co-Mo-O phase diagram provided in Fig. S7 have been taken into consideration.

The XRD diffractogram of Co100 corresponds to cobalt (II,III) oxide (JCPDS 42-1467). This material has a spinel structure, as the obtained diffraction peaks indicate. The XRD diffractogram of Mo100 corresponds to molybdenum (VI) oxide (JCPDS 05-0508). The material has an orthorhombic crystal structure. Finally, The XRD diffractogram of Co25Mo75 corresponds to cobalt molybdenum oxide (JCPDS 21-0868) which has a monoclinic crystal structure.

Catalyst	Cobalt (II,III) oxide (wt%)	Cobalt Molybdenum oxide (wt%)	Molybdenum trioxide (wt%)
Co100	100	-	-
Co80Mo20	90	10	-
Co60Mo40	56	44	-
Co25Mo75	-	100	-
Mo100	-	-	100

Table 2: Estimated composition of the cobalt and molybdenum oxides using the Reference Intensity Ratio (RIR) quantitative analysis method.

Based upon the above, it can be determined that the cobalt-rich oxides (i.e. Co80Mo20 and Co60Mo40) are composed of a mixture of cobalt (II,III) oxide and cobalt molybdenum oxide. In addition, the proportion of each phase present in each catalyst has been shown in Table 2. The proportions have been approximated through the Reference Intensity Ratio (RIR) quantitative analysis method.

3.1.3. X-ray Photoelectron Spectroscopy of the cobalt and molybdenum mixed oxides

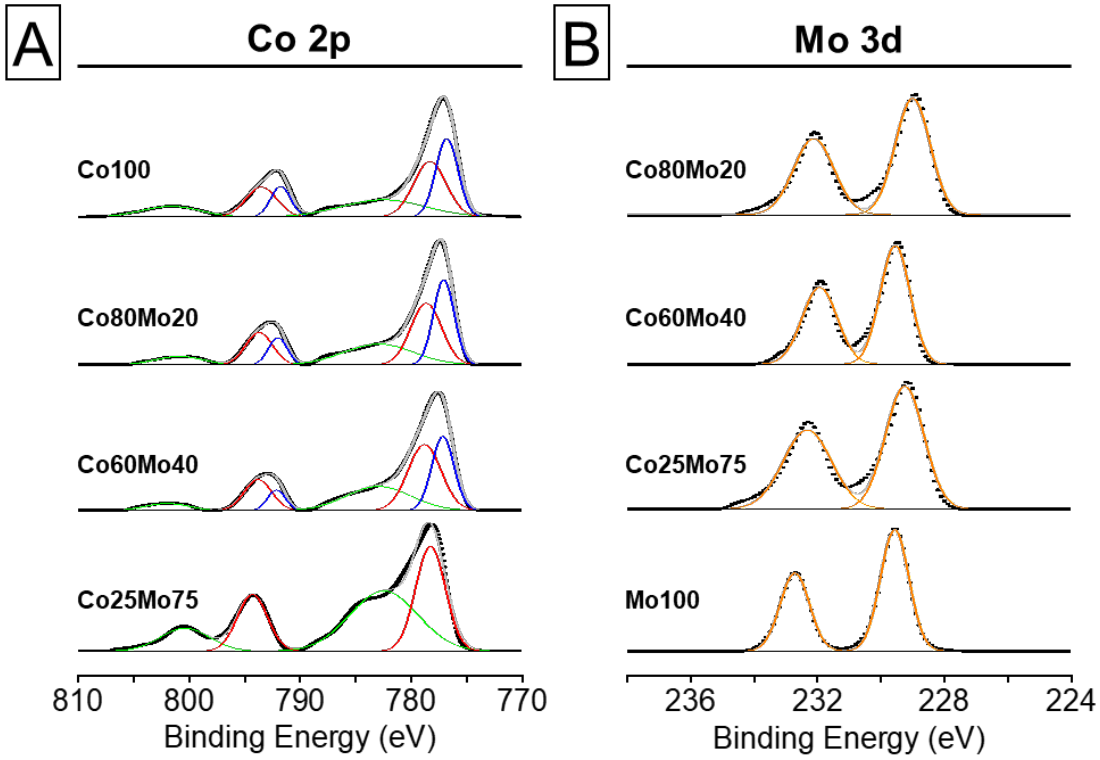

Fig. 4: Co 2p (A) and Mo3d (B) XPS spectra of the cobalt and molybdenum mixed oxides after reaction.

The surface composition and chemical states of the cobalt and molybdenum oxides were studied by X-ray Photoelectron Spectroscopy (XPS). The Co 2p and Mo 3d spectra of the cobalt and molybdenum oxides after reaction are shown in Fig. 4**.** As can be seen in Fig. 4A, the Co 2p spectra of Co100, which has been identified as pure cobalt (II,III) oxide by XRD in section 3.1.2, comprises two major peaks [33–35]. The Co $2p_{3/2}$ peak can be deconvoluted into Co^{3+} at 777.0 eV, Co^{2+} at 778.7 eV and a shakeup satellite at 783.0 eV. Similarly the Co 2p1/2 peak can be deconvoluted into Co^{3+} at 791.9 eV, Co^{2+} at 793.6 eV and a shakeup satellite at 800.6 eV. The cobalt-rich oxides, Co80Mo20 and Co60Mo40, share a similar spectra to Co100. Nevertheless it can be observed that an increased molybdenum loading results in larger peaks attributable to Co^{2+} and smaller peaks attributable to Co^{3+}. Finally, in the case of Co25Mo75, no peaks attributable to Co^{3+} can be observed. As can be seen in Fig. 4B, the Mo 3d spectra off all the molybdenum-containing oxides is similar. Their spectrum can be deconvoluted into two Mo^{6+} peaks around 229.2 and 232.3 eV [36,37]. Finally, the *Co 2p (A) and Mo3d (B) XPS spectra of the fresh catalysts were identical, as can be seen in Fig. S10.*

3.1.4. Temperature Programmed Reduction

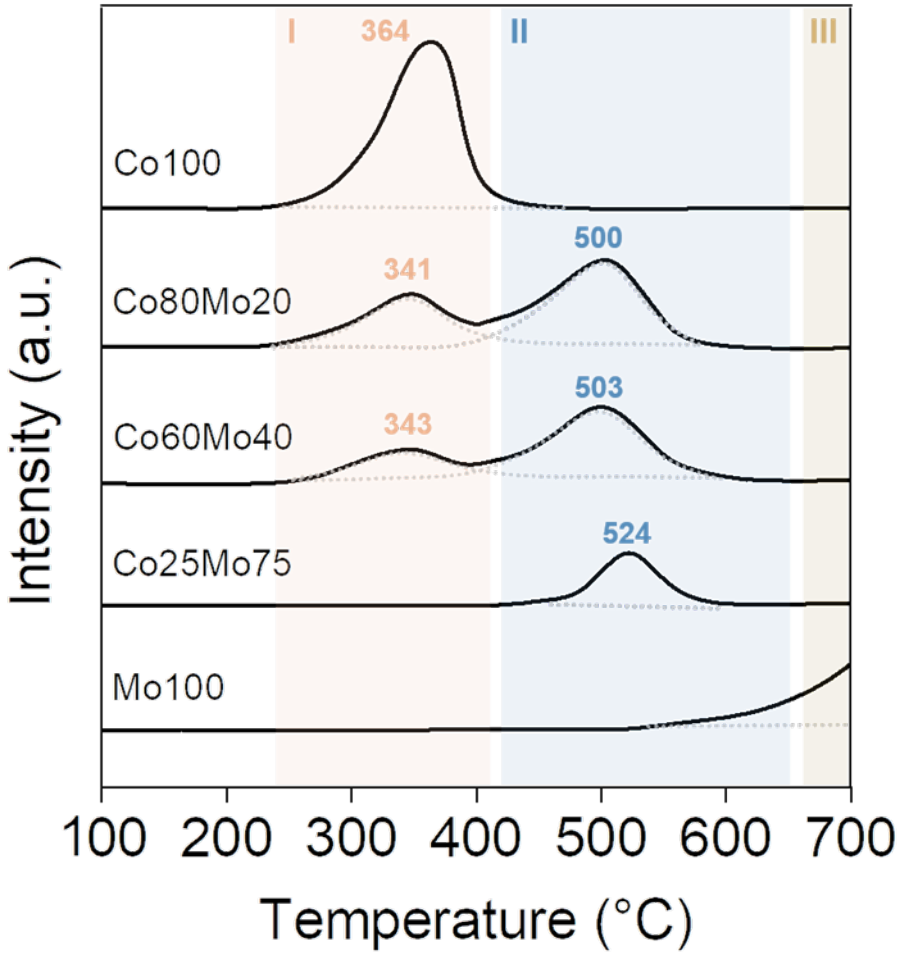

Fig. 5: TPR profiles of the cobalt and molybdenum mixed oxides. Legend: reduction of cobalt (II,III) oxide to metallic cobalt (section I), reduction of cobalt molybdenum oxide to metallic cobalt and metallic molybdenum (section II) and reduction of molybdenum (VI) oxide to molybdenum (IV) oxide (section III).

Temperature Programmed Reduction (TPR) profiles of cobalt and molybdenum mixed oxides are shown in Fig. 5. The TPR profiles of the pure oxides (i.e. Co100, Mo100 and Co25Mo75) in combination with the open literature and the Co-Mo-O phase diagram provided in Fig. S7 were used as references to interpret the profiles of the rest of the cobalt and molybdenum oxides.

Overall, the TPR profiles show three different regions: i) reduction of cobalt (II,III) oxide to metallic cobalt in the 250-420˚C temperature range [31], ii) reduction of cobalt molybdenum oxide to metallic cobalt and

metallic molybdenum in the 430-640˚C temperature range [31], and iii) reduction of molybdenum (VI) oxide to molybdenum (IV) oxide from 650˚C onwards [31].

The TPR profile of cobalt-rich oxides (i.e. Co80Mo20 and Co60Mo40) showed reduction peaks in regions I and II, attributable to the reduction of cobalt (II,III) oxide and cobalt molybdenum oxide, respectively. In both regions, the reduction peaks where observed at temperatures approximately 20°C lower when compared to the profile of the respective pure oxides, Co100 (i.e. cobalt (II,III) oxide) and Co25Mo75 (i.e. cobalt molybdenum oxide).

3.1.5. Thermogravimetric Analysis under air flow

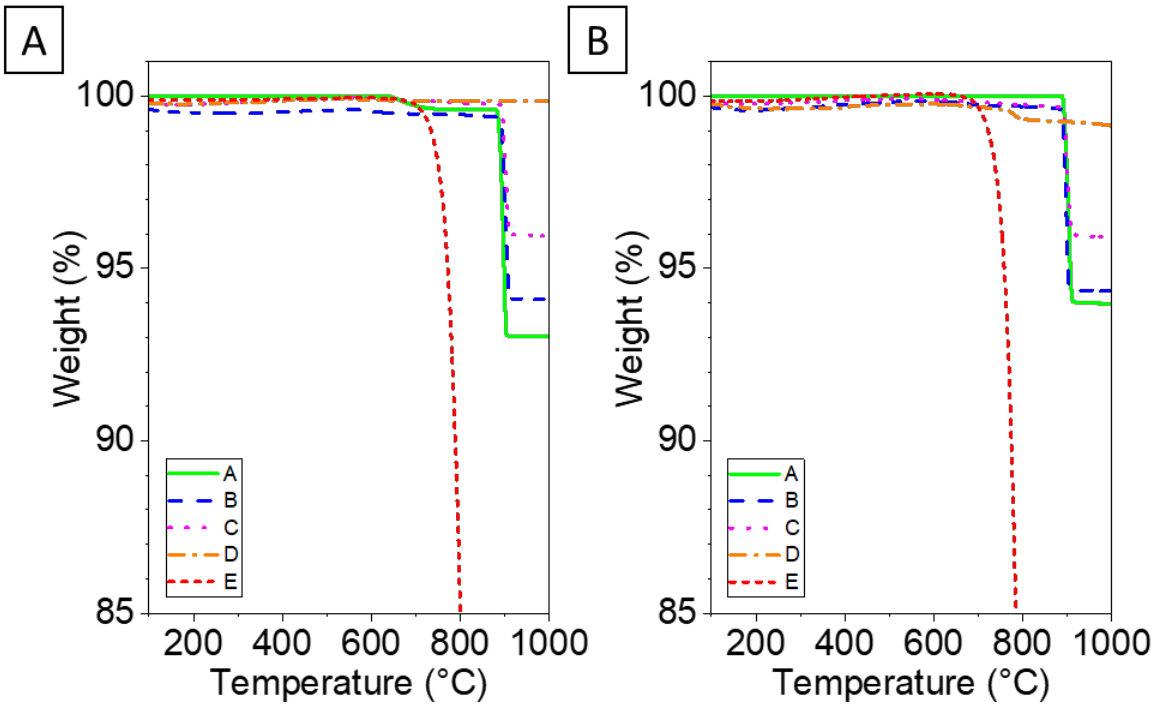

Fig. 6: TGA under flowing air of the fresh cobalt and molybdenum mixed oxides (A) and after reaction (B). Legend: Co100 (A), Co80Mo20 (B), Co60Mo40 (C), Co25Mo75 (D), and Mo100 (E).

The thermogravimetric analysis under air flow of fresh and reacted catalysts are shown in Fig. 6. As can be seen in Fig. 6, a sharp drop in mass around 900°C was observed in the profile of the cobalt-rich oxides (*i.e*. Co100, Co80Mo20 and Co60Mo40). The magnitude of the mass drop was the largest for Co100 (i.e. 7%), followed by Co80Mo20 (*i.e.* 6%) and, finally, by Co60Mo40 (*i.e.* 4%). The profile of these three oxides after reaction was similar to that of the respective fresh catalysts. In the case of Mo100 the mass

drop, which started around 650°C, was of 66%, both when a fresh and a reacted sample were used. In contrast, the profiles of fresh and reacted Co25Mo75 show a different profile. It can be seen in Fig. 6 that the mass of Co25Mo75 was fairly stable throughout the entire experiment, whereas after the reaction it experienced a slight drop, of 0.2%, around 775-800°C.

3.1.6. Scanning Electron Microscopy and Energy Dispersive X-ray Spectroscopy of the cobalt and molybdenum mixed oxides

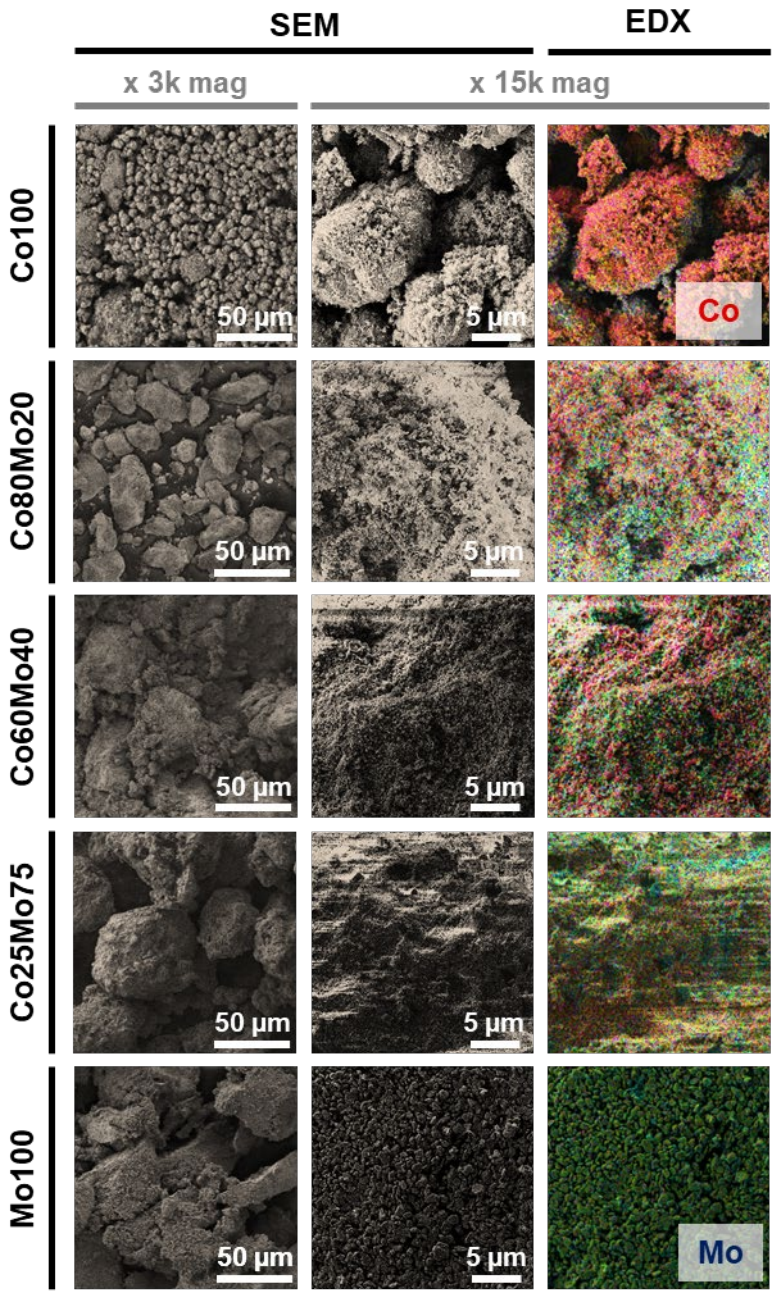

Fig. 7: SEM images and EDX surface mapping of the fresh cobalt and molybdenum mixed oxides. Legend: cobalt (red) and molybdenum (blue).

The morphology and the elemental analysis of cobalt and molybdenum oxides were studied by Scanning Electron Microscopy (SEM) and Energy Dispersive X-ray Spectroscopy (EDX) surface mapping, respectively, see Fig. 7. Low magnification SEM images show that the grain size of Mo100 (i.e. 100 µm) was two orders of magnitude larger than that of Co100 (i.e. 5 µm). As a general trend, it can be observed that an increase in molybdenum content resulted in an increase in the grain size. As a result, the morphology of Co100 and Co80Mo20 was composed of small and loose round-shaped particles whereas that of Mo100 consisted of agglomerated and asymmetric angular-shaped particles. Nevertheless, it is important to highlight that the particle size of Co80Mo20 was 5 times larger than that of Co100, 25 and 5 µm, respectively. It is worth mentioning that the catalysts' morphology was not affected by the reaction conditions, as can be seen in *Fig. S11.* Finally, the EDX surface mapping analysis shown in Fig. 7 indicated that cobalt and molybdenum were uniformly distributed.

3.2. Performance studies of the cobalt and molybdenum mixed oxides during the total oxidation of methane

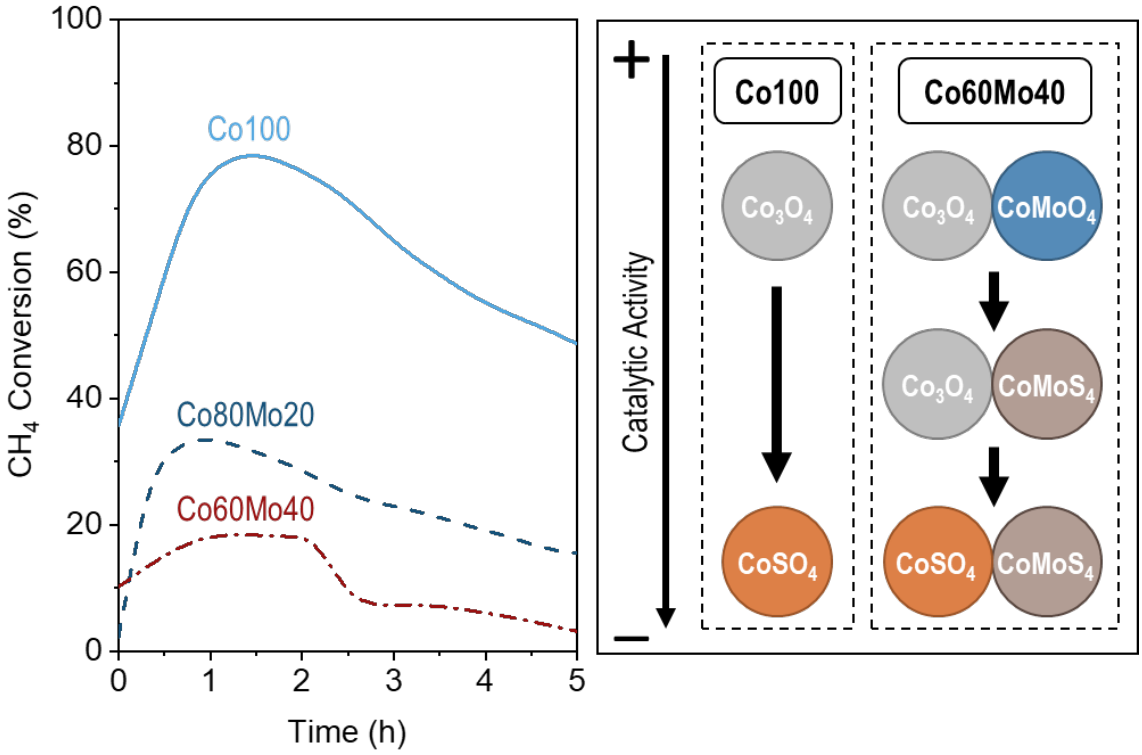

Fig. 8: Stability studies of the cobalt and molybdenum catalysts at 450°C under 312 ppmV of methane, 4.6 ppmV of sulfur dioxide, and 10%vol steam balanced in air (Left) and proposed poisoning mechanism (Right).

The performance of cobalt and molybdenum oxides during the total oxidation of methane under typical exhaust conditions of a natural gas turbine are shown in Fig. 8. As a general trend, as the molybdenum loading was increased, the methane conversion levels dropped. In fact, only the cobalt-rich catalysts (i.e. Co100, Co80Mo20 and Co60Mo40) presented some degree of activity. Among the three active catalysts, the maximum methane conversion achieved at 450°C decreased in the following order: Co100 > Co80Mo20 > Co60Mo40.

As can be seen in the conversion profiles shown in Fig. 8, two different behaviours can be observed for the active catalysts. In the case of catalysts Co100 and Co80Mo20, initially the methane conversion levels experienced a rise until a maximum point was reached, which lead to a gradual decrease in methane conversion levels throughout the rest of the experiment. In contrast, in the case of catalyst Co60Mo40 the initial rise in methane conversion levels was followed by a 1 h plateau in methane conversion levels. Subsequently, a sharp drop in methane conversion levels was observed and, finally, a gradual decrease in methane conversion levels was observed for the rest of the experiment.

3.3. In situ Diffuse Reflectance Infrared Fourier Transform Spectroscopy

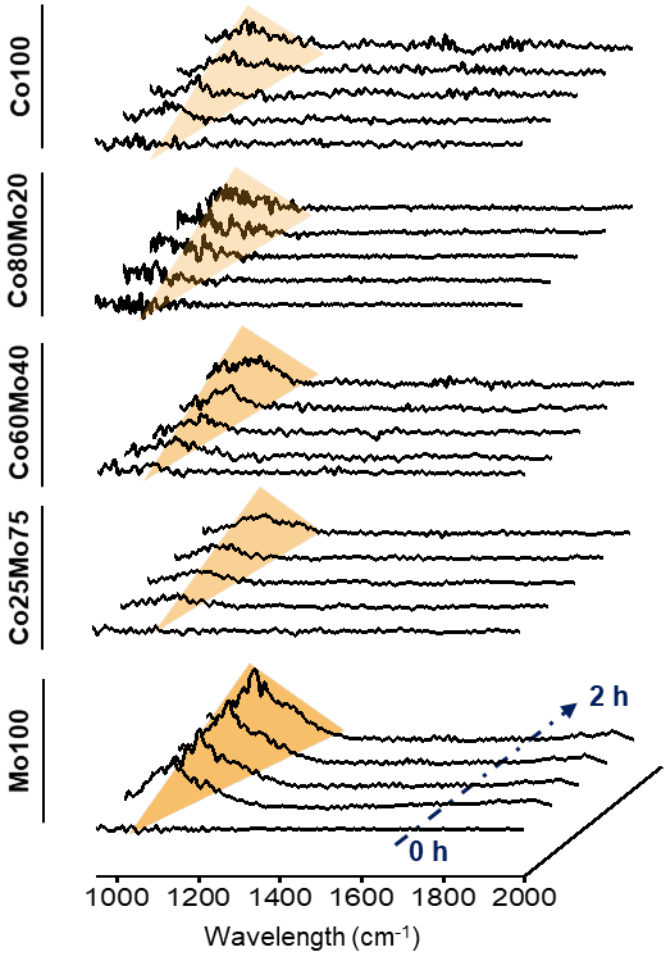

Fig. 9: In situ DRIFTS spectra of the cobalt and molybdenum oxides at 450°C in the presence of 347 ppmV of methane and 5.1 ppmV of sulfur dioxide balanced in air.

In order to study the reaction mechanisms during the total oxidation of methane, the surface chemistry of cobalt and molybdenum oxides was evaluated using *in situ* Diffuse Reflectance Infrared Fourier Transform Spectroscopy (DRIFTS).

As can be seen in Fig. 9, after two hours under sulfur dioxide-containing reaction conditions all the catalysts developed a large IR band in the 1000-1200 cm^{-1} range that can be attributed, according to the literature, to the presence of sulfate species [13,38]. The band was particularly noticeable for Co60Mo40, Co25Mo75 and Mo100.

3.4. Performance studies of the hollow fibre-based reactor during the total oxidation of methane

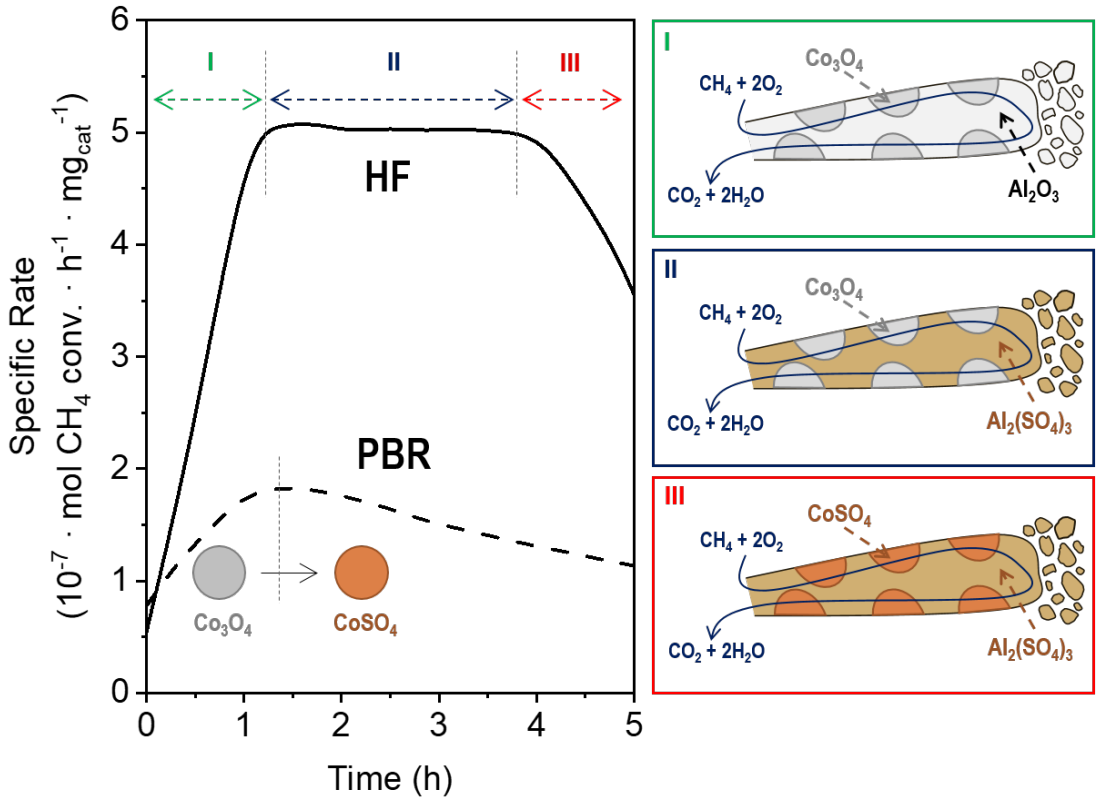

Fig. 10: Normalised stability studies of the Co100 packed bed reactor and Co100 hollow fibre-based reactor at 450°C under 312 ppmV of methane, 4.6 ppmV of sulfur dioxide, and 10%vol steam balanced in air (Left) and proposed poisoning mechanism (Right). The non-normalised version of this plot is shown in Fig. S12.

The effect of an alumina hollow fibre as a micro-structured catalyst support and sulfur sink was studied in this section. Among the studied catalysts, Co100 was chosen as the best candidate to be impregnated into the hollow fibre due to its high activity and low resistance to sulfur dioxide. As can be seen in Fig. 10, the conversion of methane per mg of catalyst increased 3-fold when using an alumina hollow fibre support in comparison to a bulk catalyst. In addition, the rise in methane conversion levels and subsequent decrease in methane conversion levels were sharper in the case of the supported catalyst. Finally, stable methane conversion levels where observed during the 1.5 h to 4 h interval. Note that a longer 15 h experiment showing the complete loss of activity of Co100 for both the hollow fibre-based reactor and the packed bed reactor has been included in Fig. S13.

3.5. X-ray Photoelectron Spectroscopy of the hollow fibre-based reactor

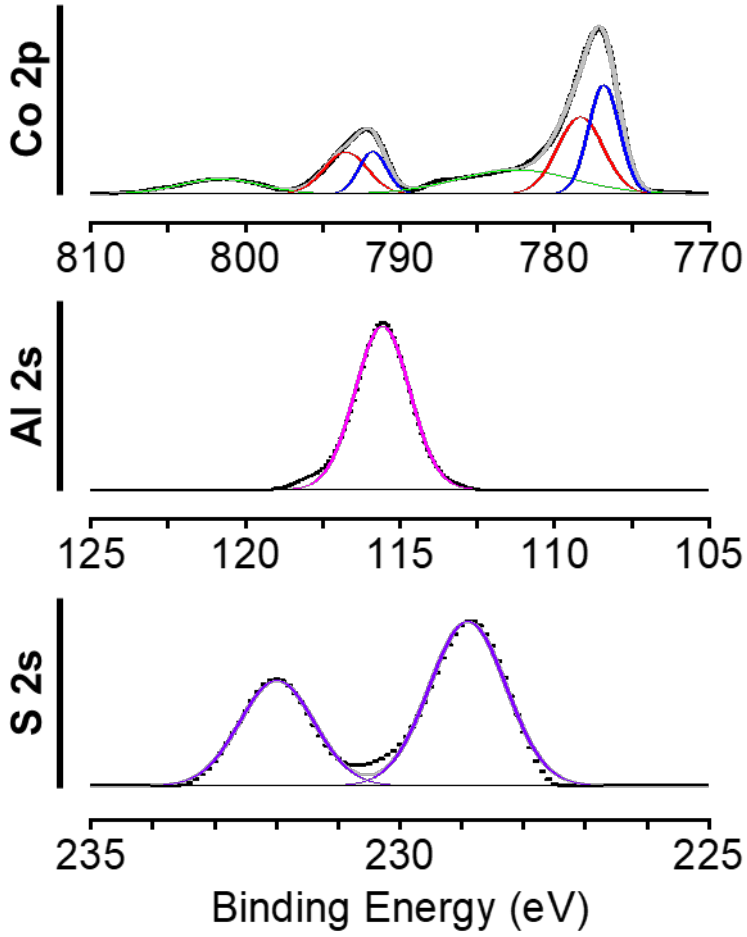

Fig. 11: XPS spectra of the hollow fibre-based reactor impregnated with Co100 after reaction.

The surface composition and chemical states of the hollow fibre-based reactor were studied by X-ray Photoelectron Spectroscopy (XPS). As can be seen in Fig. 11, the Co 2p XPS spectra of the hollow fibre-based reactor was identical to that of Co100, which has been described in section 3.1.3. In addition, the Al 2s spectra shows a single Al peak at 115.5 eV. Finally, the S 2s spectra can be deconvoluted into two peaks at 228.9 eV and 232.0 eV.

3.6. Scanning Electron Microscopy and Energy Dispersive X-ray Spectroscopy of the hollow fibre-based reactor

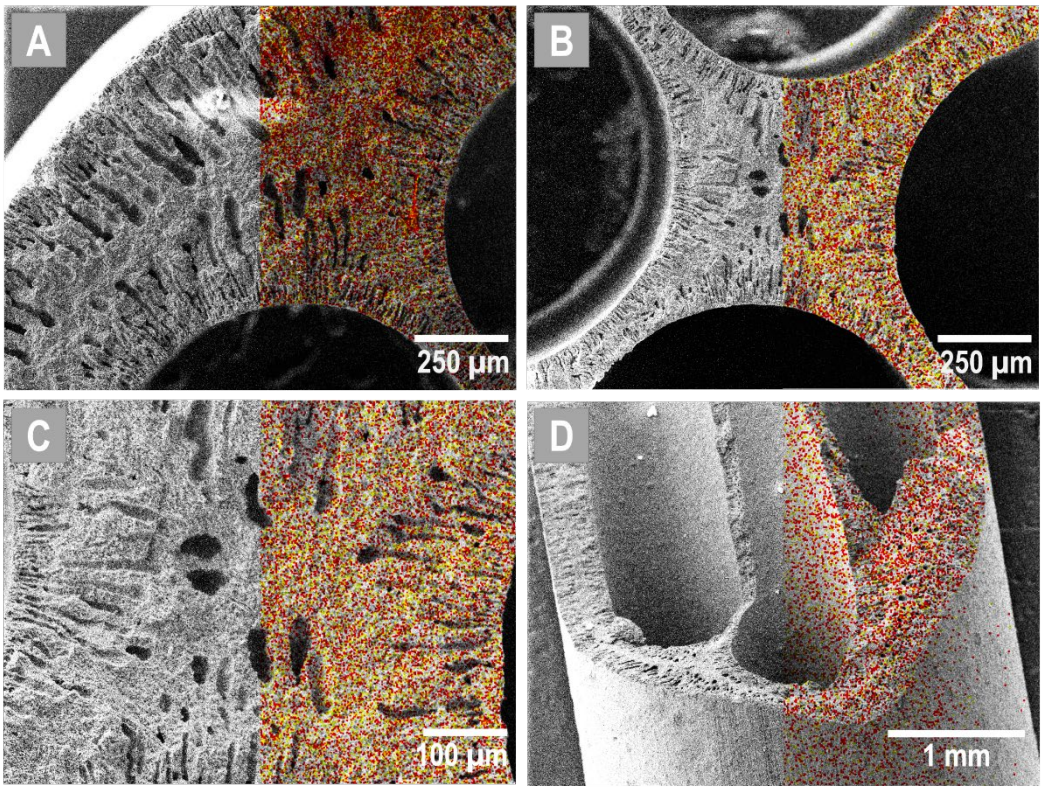

Fig. 12: SEM images and EDX surface mapping of the hollow fibre-based reactor impregnated with Co100. Legend: cobalt (red) and sulfur (yellow).

Scanning electron microscopy (SEM) and energy dispersive X-ray spectroscopy (EDX) presented in Fig. 12 show the morphology and chemistry of the hollow fibre-based reactor after reaction. The SEM images show that the 4-channel asymmetric hollow fibre exhibits a 'sandwich' structure. The 'sandwich' structure of the hollow fibre fingers is particularly noticeable in Fig. 12A.

The EDX surface mapping images indicate that the Co100 catalyst was homogeneously distributed throughout the fibre. In addition, a signal attributable to sulfur was also identified. As can be seen in Fig. 12D, the signal was stronger in the internal structure of the hollow fibre-based reactor.

4. Discussion

4.1. Characterisation of the cobalt and molybdenum mixed oxides

4.1.1. Nitrogen Adsorption/Desorption Isotherms

As can be seen in Fig. 2B, BET surface areas of mixed oxides were larger than those of the pure oxides and are similar to those reported in the literature [4,39–41]. Although this trend is widely reported in the literature, to the best of our knowledge, an explanation for this phenomenon has not yet been given. In this respect, Choya et al. [4] reported that the surface area of cobalt (II,III) oxide doped with cerium (IV) oxide was twice larger than that of un-doped cobalt (II,III) oxide, 35 m^2 g^{-1} and 14 m^2 g^{-1}, respectively. The authors proposed that the addition of ceria caused a distortion in the spinel structure of cobalt (II,III) oxide which increased its lattice parameters and decreased its crystallite size. A similar phenomenon could explain the increase in the surface area of the cobalt and molybdenum oxides presented herein.

4.1.2. X-ray Powder Diffraction

The XRD diffractogram of the cobalt and molybdenum mixed oxides here studied revealed that oxides Co100, Mo100 and Co25Mo75 corresponded to pure oxides, cobalt (II,III) oxide, molybdenum (VI) oxide and cobalt molybdenum oxide, respectively. However, the other two oxides, Co80Mo20 and Co60Mo40, were composed of a mixture of oxides in varying compositions, as indicated in Table 2.

The obtained XRD diffractograms identified using the ICDD database Powder Diffraction Files (PDF-3) agreed with the literature [4,41–43]. The XRD diffractogram of Co100 was similar to that reported by Choya et al. [4], that of Co25Mo75 to that reported by Moura et al. [42] and that of Mo100 to that reported by Hu et al [43]. Likewise, Shim et al. [41] also observed the presence of cobalt (II,III) oxide and cobalt molybdenum oxide phases in unsupported cobalt and molybdenum oxides, which agrees with the XRD diffractograms of Co80Mo20 and Co60Mo40 here studied.

The XRD diffractogram of the catalysts after reaction shown in Fig. S9 did not show signs of sulfates. This suggests that the sulfates leading to the deactivation of the catalysts are only formed in very small proportions on the surface and do not affect the catalysts' bulk structure.

4.1.3. X-ray Photoelectron Spectroscopy of the cobalt and molybdenum mixed oxides

The XPS spectra presented in Fig. 4 agree with the results obtained from the XRD characterisation as well as the open literature [33–37]. As can be seen in Fig. 4A, the Co 2p spectra of the cobalt-rich oxides

shows that an increased molybdenum content results in a larger presence of Co^{2+} cations, which can particularly be observed in the growth of the shakeup satellite at 783.0 eV [44]. Taking into account the results from XRD characterisation (section 3.1.2.) these can be attributed to a larger presence of cobalt molybdenum oxide. In addition, a comparison between the cobalt and molybdenum oxides before and after reaction does not indicate a larger proportion of Co^{2+} cations attributable to cobalt (II) sulfate after reaction. Nevertheless, the deactivation of the catalysts observed in Fig. 8 indicates that sulfur dioxide is poisoning the catalysts. Therefore, it can be concluded that the low concentration of sulfur dioxide (i.e. 4.6 ppmV) and the short ageing time (i.e. 5 h) used in this study did not generate enough surface sulfates to surpass the detection limit of the spectrometer. Furthermore, no peaks attributable to Mo^{4+} were observed in the Mo 3d spectra of the molybdenum-containing oxides. The presence of Mo^{4+} would confirm that molybdenum disulfide had been generated on the surface of the catalysts after reaction.

4.1.4. Temperature Programmed Reduction

The reduction peaks of Co80Mo20 and Co60Mo40 were observed at a lower temperature than for Co100 and Co25Mo75, as can be seen in Fig. 5. This phenomenon has been explained by Halawy et al. [31] who reported that traces of metallic cobalt formed at low temperatures, can act as catalytic centres, contributing towards an autocatalytic process that facilitates hydrogen dissociation.

4.1.5. Thermogravimetric Analysis under air flow

The thermogravimetric analysis under air flow provided additional information on the composition of the cobalt and molybdenum oxides here studied. Fig. 5 shows a mass drop around 900°C for cobalt-rich mixed-oxides corresponding to the reduction of cobalt (II,III) oxide to cobalt (II) oxide [45]. Notice that the mass drop was proportional to the amount of cobalt (II,III) oxide present in each catalyst, being most noticeable for Co100. On the other hand, the large mass drop observed for Mo100 accounted for the sublimation of molybdenum (VI) oxide [46,47]. Finally, the fact that Co25Mo75 did not experience a mass drop throughout the entire temperature range suggest that the cobalt molybdenum oxide phase has a high thermal stability. Nevertheless, it is important to highlight that this post-reaction sample presented a 0.2% mass drop observed around 775-800°C, which could be tentatively attributed to the desorption of surface sulfates [13].

4.1.6. Scanning Electron Microscopy and Energy Dispersive X-ray Spectroscopy of the cobalt and molybdenum mixed oxides

Similar SEM images to those presented in Fig. 7 have been reported in the open literature for pure cobalt (II,III) oxide [13], pure molybdenum (VI) oxide [48] and cobalt and molybdenum mixed oxides [40].

SEM images suggest that there is not a link between the particle size and the BET surface area. In this respect, Co100 and Mo100, which had the smallest and the largest particle sizes, respectively, had the lowest surface areas among all the oxides here studied. As a result, the relatively large BET surface area of the cobalt and molybdenum oxides is likely to originate from the larger pore volume of the particles, as can be seen in Table 1.

It was observed that an increase in molybdenum content resulted in an increase in the grain size of the cobalt and molybdenum oxides. Based upon Pauling's concept of electronegativity, the higher electronegativity of molybdenum when compared to cobalt could explain the larger grain size of the molybdenum-containing oxides observed in Fig. 7.

Finally, the uniform distribution of cobalt and molybdenum observed by EDX further confirms the presence of a mixed metal oxide, which is in agreement with XRD results.

4.2. Performance studies of the cobalt and molybdenum mixed oxides during the total oxidation of methane

The performance studies suggest that the catalytic activity of cobalt and molybdenum oxides depends on their crystal phase. Cobalt-rich oxides (i.e. Co100, Co80Mo20 and Co60Mo40), which contain a cobalt spinel (i.e. cobalt (II,III) oxide) are highly active for the total oxidation of methane. However, cobalt-poor oxides (i.e. Co25Mo75 and Mo100), which do not contain the cobalt spinel are not active under the studied reaction conditions. This can be explained due to the presence of Co^{3+} cations in the cobalt spinel which are known to be highly reactive for the total oxidation of methane due to their good redox properties. In contrast, Co^{2+} cations present in cobalt-poor oxides (i.e. cobalt molybdenum oxide), are not easily reducible compromising the catalytic activity due a decrease in the mobility of lattice oxygen [4].

It is important to highlight the difference in the performance of Co60Mo40 with respect to that of Co100 and Co80Mo20. As can be seen in Fig. 8, the conversion profile of Co60Mo40 shows a plateau followed by a sharp drop in the methane conversion, which suggests that this catalyst has a higher resistance to sulfur-induced deactivation. This could be explained due to Co60Mo40 containing 44 wt% cobalt molybdenum oxide phase, a well-known sulfur sink that delays sulfur-induced poisoning. The sulfur sink effects of this phase have been studied by Rodriguez et al. [25], who found that cobalt molybdenum oxide is a good sorbent for sulfur dioxide. In addition, this study found that the presence of steam enhaced the

formation of sulfided cobalt molybdenum oxide. This indicates that, eventhough cobalt molybdenum oxide is not catalytically active, this phase can be responsible for extending the life of sulfur-sensitive catalysts.

Furthermore, there is a link between the particle size of the cobalt-rich oxides and their catalytic activity: the smaller the particle size, the higher the catalytic activity is. This difference in the catalytic activity could also be attributed to the difference in cobalt spinel content. Moreover, the fact that the larger surface area of Co80Mo20 and Co60Mo40 does not enhance their catalytic activity suggests that this reaction might be internal diffusion limited under the studied reaction conditions.

Finally, Fig. 8 shows the sharp rise in methane conversion experienced by catalysts Co100 and Co80Mo20 during the first 60-90 min, which can be explained by an increased surface area due to the formation of sulfates. The presence of traces of sulfur dioxide gives rise to two competitive behaviours, which can be explained in the following way. On one hand, sulfur dioxide increases the surface area of the cobalt-rich catalysts due to the formation of a cobalt sulfate. As can be seen in Table 1, the surface area of Co100 increases 4-fold during the first hour. This results in more catalytic surface being available for the total oxidation of methane, increasing the performance of the catalyst. Similar behaviour has been reported by Ordóñez et al. [13] for chromium oxide-based catalysts under similar reaction conditions during the total oxidation of methane. On the other hand, the same sulfur dioxide is gradually poisoning the catalyst, resulting in a gradual loss of catalytic activity. As can be seen in Fig. 8, after 75 min of reaction, the benefit of larger surface area is overtaken by the poisoning effect of sulfur dioxide. This deactivation is similar to that typically reported for PGM metals supported on a non-sulfating supports such as SiO_2. In contrast, the delayed deactivation of Co60Mo40 resembles that of PGM metals supported on a sulfating support such as Al_2O_3 [9]. Moreover, the most active catalyst of this study, Co100 (i.e. Cobalt (II,III) oxide), has been compared in terms of activity to both PGM and non-PGM catalysts in Table 3.

PGM Catalysts			
Catalyst/support	Feed Including	Normalised Reaction Rate*	Ref. (year)
PdO/ zeolite	10 ppmV SO_2, 5%vol H_2O	3.87E-05	[49] (2019)
Pt-Pd/Al_2O_3	10 ppmV SO_2, 5%vol H_2O	9.57E-05	[38] (2018)
Pt/Al-Mn-Ce	10 ppmV SO_2, 12.5%vol H_2O	1.17E-05	[50] (2020)
Non-PGM Catalysts			
Catalyst/support	Feed Including	Normalised Reaction Rate*	Ref. (year)
Cr_2O_3 (bulk)	25 ppmV H_2S, 2%vol H_2O	1.20E-05	[13] (2008)
Fe_2O_3-Cr_2O_3 (bulk)	4.6 ppmV SO_2, 10%vol H_2O	2.35E-06	[14] (2020)
Co_3O_4 (bulk)	4.6 ppmV SO_2, 10%vol H_2O	2.50E-06	-

*Table 3: Comparison of the catalysts presented in this study with recent published studies in the field of total methane oxidation. *Normalised Reaction Rate units: mol CH_4 conv. / s · mg_{cat} · mol CH_4 · L^{-1} (i.e.*

conversion rate normalised by the mass of catalyst and the concentration of methane present in the feed). Note that initial/maximum conversion rates have been used to calculate the normalised reaction rate.

4.3. In situ Diffuse Reflectance Infrared Fourier Transform Spectroscopy

In situ DRIFTS experiments under the reaction conditions indicate that cobalt and molybdenum oxides show different affinities towards sulfur dioxide. The growth of IR bands attributable to sulfates in the 1000-1200 cm^{-1} range, suggest that the molybdenum (VI) oxide and the cobalt molybdenum oxide have a higher affinity towards sulfur dioxide than the cobalt (II,III) oxide. These results agree with Rodriguez et al. [16,25], who have also reported an interaction between sulfur dioxide and both molybdenum (VI) oxide and cobalt molybdenum oxide at a similar temperature range (i.e. 350-400°C).

No sulfates were identified for the two catalysts containing cobalt (II,III) oxide, Co100 and Co80Mo20. However, as can be seen in Fig. 8**,** these catalysts were severely deactivated in the presence of 4.6 ppmV of sulfur dioxide**.** Similar results have been reported by Ordóñez et al. [13], who suggested that cobalt (II,III) oxide undergoes irreversible deactivation in the presence of sulfur dioxide due to the formation of stable surface sulfates. Although, it is likely that Co100 and Co80Mo20 suffered a similar deactivation, the low concentration of sulfur dioxide (i.e. 5.1 ppmV) in the reactant mixture and the short reaction time (i.e. 2 h) made it very difficult to observe noticeable IR band growths.

4.4. Performance studies of the hollow fibre-based reactor during the total oxidation of methane

The higher performance of the hollow fibre-based reactor compared to the packed bed reactor (i.e. 3 times higher methane conversion per mg of catalyst) can be explained by a combination of two factors: (i) intensified contact between the reactants and the catalyst and (ii) sulfur-sink effects of the alumina delaying the poisoning of the active phase. The geometry of the micro-structured alumina hollow fibre leads to an ideal dispersion of the active phase, which improves the residence time distribution and minimises internal and external diffusion limitations enhancing the efficiency of the catalyst [20,21]. In addition, the sulfur sink properties of alumina [10,11,19] increase the lifetime of the catalyst. As a result, the shape of the conversion profile of the hollow fibre-based reactor shows a 2.5 h conversion plateau followed by sharp drop in methane conversion levels. The sharp drop suggests that the alumina has reached its saturation point leading to the poisoning of the active phase. Finally, the poisoning effect of sulfur dioxide leads to the complete deactivation of the active phase for both the packed bed reactor and the hollow fibre reactor experiments in under 15 h, as can be seen in Fig. S13. It is worth mentioning that

the deactivation of Co100 in the packed bed reactor experiment agrees with the typical trend reported in the literature [13].

4.5. X-ray Photoelectron Spectroscopy of the hollow fibre-based reactor

As can be observed in Fig. 10, the hollow fibre-based reactor suffered from a delayed sulfur-induced deactivation. This delay is a direct effect of the sulfur sink properties of alumina confirmed by the two peaks observed in the S 2s region of the XPS spectra, which indicate the presence of sulfates in the hollow fibre-based reactor after the 5 h reaction.

4.6. Scanning Electron Microscopy and Energy Dispersive X-ray Spectroscopy of the hollow fibre-based reactor

EDX surface mapping images showed that the morphology of the hollow fibre and the use of a liquid catalyst solution result in the catalyst being homogeneously dispersed. This impregnation method in combination with the geometry of the support overcome the major limitation faced by traditional monoliths, catalyst accumulation on the walls of the substrate [26,51]. Furthermore, EDX surface mapping analysis revealed the presence of sulfur, which suggests that the alumina hollow fibre acts as a sulfur sink, storing sulfur in the form of $Al_2(SO_4)_3$ [8,52].

5. Conclusion

This study has found that the crystal phase is the main factor affecting the catalytic activity of cobalt and molybdenum oxides during the total oxidation of methane. It has been found that under the reaction conditions here studied only the catalyst containing the cobalt (II,III) oxide phase are active. Their maximum methane conversion levels decreased with an increased molybdenum load in the following order: Co100 > Co80Mo20 > Co60Mo40. Moreover, it has been found that the cobalt molybdenum oxide phase is not active towards the total oxidation of methane. However, this phase contributes towards the overall performance of the catalyst by acting as a sulfur sink, as confirmed by the in-situ DRIFTS, slowing down the inevitable sulfur dioxide-induced poisoning of the cobalt (II,III) oxide phase.

In addition, it has been found that the use of an alumina hollow fibre as a support for pure cobalt (II,III) oxide catalyst enhances its performance and delays the poisoning of the active phase during the total

oxidation of methane under realistic conditions. The alumina hollow fibre support not only provides a large surface area, maximising the efficiency of the available catalyst, but also acts as a sulfur sink, delaying the sulfur dioxide-induced deactivation of the catalyst.

6. Acknowledgements

This work was supported by the funding provided by The Carnegie Trust for the Universities of Scotland (grant RIG008664) and The University of Edinburgh Impact Acceleration Account (EPSRC grant J27318). Moreover, M. García-Vázquez gratefully acknowledges the funding provided by the School of Engineering at the University of Edinburgh to carry out his PhD. Likewise, D. Satir gratefully acknowledges the funding provided by the Careerwise Equate Scotland to carry out her summer placement during 2019 at the Denbigh Lab at the School of Engineering at the University of Edinburgh. Finally, F. R. García-García would like to thank T. Glen, School of Physics and Astronomy at the University of Edinburgh, for his help and support with SEM image acquisition using the Cryo FIB/SEM (EPSRC grant EP/P030564/1) as well as J. M. González-Carballo and R. Tooze, Drochaid Research Services, Scotland, for their help with XRD and TPR characterisation of the catalysts. The prolegomena of this work was presented as an oral communication in the IV UKEM Workshop in October 2020 (https://emissioncontrolukem.wordpress.com/). F. R. García-García would like to thank all who attended that session for their helpful comments and discussion.

7. References

[1] S.H. Mohr, J. Wang, G. Ellem, J. Ward, D. Giurco, Fuel 141 (2015) 120–135.

[2] NTEL, Cost and Performance Baseline for Fossil Energy Plants Volume 1b: Bituminous Coal (IGCC) to Electricity, 2015.

[3] S. Schwietzke, W.M. Griffin, H.S. Matthews, L.M.P. Bruhwiler, Environ. Sci. Technol. 48 (2014) 7714–7722.

[4] A. Choya, B. de Rivas, J.R. González-Velasco, J.I. Gutiérrez-Ortiz, R. López-Fonseca, Appl. Catal. B Environ. 237 (2018) 844–854.

[5] T.N. Lavoie, P.B. Shepson, C.A. Gore, B.H. Stirm, R. Kaeser, B. Wulle, D. Lyon, J. Rudek, Environ. Sci. Technol. 51 (2017) 3373–3381.

[6] A. Yasar, R. Haider, A.B. Tabinda, F. Kausar, M. Khan, Polish J. Environ. Stud. 22 (2013) 1277–

1281.

[7] N.M. Kinnunen, M. Keenan, K. Kallinen, T. Maunula, M. Suvanto, ChemCatChem 10 (2018) 1556–1560.

[8] N.M. Kinnunen, V.H. Nissinen, J.T. Hirvi, K. Kallinen, T. Maunula, M. Keenan, M. Suvanto, Catalysts 9 (2019) 427.

[9] A. Gremminger, P. Lott, M. Merts, M. Casapu, J.D. Grunwaldt, O. Deutschmann, Appl. Catal. B Environ. 218 (2017) 833–843.

[10] L.J. Hoyos, H. Praliaud, M. Primet, Appl. Catal. A Gen. 98 (1993) 125–138.

[11] P. Gélin, M. Primet, Appl. Catal. B Environ. 39 (2002) 1–37.

[12] J. Zhang, D. Tan, Q. Meng, X. Weng, Z. Wu, Appl. Catal. B Environ. 172–173 (2015) 18–26.

[13] S. Ordóñez, J.R. Paredes, F. V. Díez, Appl. Catal. A Gen. 341 (2008) 174–180.

[14] M. García-Vázquez, K. Wang, J.M. González-Carballo, D. Brown, P. Landon, R. Tooze, F.R. García-García, Appl. Catal. B Environ. 277 (2020) 119139.

[15] J. Wallace, Wall Str. J. (2020).

[16] J.A. Rodriguez, S. Chaturvedi, J.C. Hanson, J.L. Brito, J. Phys. Chem. B 103 (1999) 770–781.

[17] J.G. Speight, Natural Gas : A Basic Handbook, n.d.

[18] A. Raj, Johnson Matthey Technol. Rev. 60 (2016) 228–235.

[19] M. García-Vázquez, G. Zhang, Z. Hong, X. Gu, F.R. García-García, Chem. Eng. J. 396 (2020) 125379.

[20] F.R. García-García, K. Li, Appl. Catal. A Gen. 456 (2013) 1–10.

[21] F.R. García-García, S.C. Tsang, K. Li, J. Memb. Sci. 455 (2014) 92–102.

[22] G.M. Bremmer, L. van Haandel, E.J.M. Hensen, J.W.M. Frenken, P.J. Kooyman, Appl. Catal. B Environ. 243 (2019) 145–150.

[23] M. Egorova, R. Prins, J. Catal. 241 (2006) 162–172.

[24] H. Nava, C. Ornelas, A. Aguilar, G. Berhault, S. Fuentes, G. Alonso, Catal. Letters 86 (2003) 257–265.

[25] J.A. Rodriguez, J.C. Hanson, S. Chaturvedi, J.L. Brito, Stud. Surf. Sci. Catal. 130 C (2000) 2795–2800.

[26] N.I. Mahyon, T. Li, R. Martinez-Botas, Z. Wu, K. Li, Catal. Commun. 120 (2019) 86–90.

[27] Z. Chen, S. Wang, W. Liu, X. Gao, D. Gao, M. Wang, S. Wang, Appl. Catal. A Gen. 525 (2016) 94–102.

[28] Z. Pu, H. Zhou, Y. Zheng, W. Huang, X. Li, Appl. Surf. Sci. 410 (2017) 14–21.

[29] F. Zasada, J. Janas, W. Piskorz, M. Gorczyńska, Z. Sojka, ACS Catal. 7 (2017) 2853–2867.

[30] A. Choya, B. de Rivas, J.R. González-Velasco, J.I. Gutiérrez-Ortiz, R. López-Fonseca, Appl. Catal. A Gen. 591 (2020).

[31] S.A. Halawy, M.A. Mohamed, G.C. Bond, J. Chem. Technol. Biotechnol. 58 (1993) 237–245.

[32] Z. Shi, Y. Zhang, C. Cai, C. Zhang, X. Gu, Ceram. Int. 41 (2015) 1333–1339.

[33] J. Bae, D. Shin, H. Jeong, B.S. Kim, J.W. Han, H. Lee, ACS Catal. 9 (2019) 10093–10100.

[34] Y. Cai, J. Xu, Y. Guo, J. Liu, ACS Catal. 9 (2019) 2558–2567.

[35] M. Zhao, J. Deng, J. Liu, Y. Li, J. Liu, Z. Duan, J. Xiong, Z. Zhao, Y. Wei, W. Song, Y. Sun, ACS Catal. 9 (2019) 7548–7567.

[36] J. Zhao, X. Ren, H. Ma, X. Sun, Y. Zhang, T. Yan, Q. Wei, D. Wu, ACS Sustain. Chem. Eng. 5 (2017) 10093–10098.

[37] W. Xie, T. Yu, Z. Ou, J. Zhang, R. Li, S. Song, Y. Wang, ACS Sustain. Chem. Eng. 8 (2020) 9070–9078.

[38] N. Sadokhina, G. Smedler, U. Nylén, M. Olofsson, L. Olsson, Appl. Catal. B Environ. 236 (2018) 384–395.

[39] E. Furimsky, C.H. Amberg, Can. J. Chem. 53 (1975) 2542–2547.

[40] M.L. Vrinat, L. De Mourgues, Appl. Catal. 5 (1983) 43–57.

[41] J.O. Shim, D.W. Jeong, W.J. Jang, K.W. Jeon, S.H. Kim, B.H. Jeon, H.S. Roh, J.G. Na, Y.K. Oh, S.S. Han, C.H. Ko, Catal. Commun. 67 (2015) 16–20.

[42] A.P. de Moura, L.H. de Oliveira, P.F.S. Pereira, I.L. V. Rosa, M.S. Li, E. Longo, J.A. Varela, Adv. Chem. Eng. Sci. 02 (2012) 465–473.

[43] H. Hu, C. Deng, J. Xu, K. Zhang, M. Sun, J. Exp. Nanosci. 10 (2015) 1336–1346.

[44] L. Lukashuk, K. Föttinger, E. Kolar, C. Rameshan, D. Teschner, M. Hävecker, A. Knop-Gericke, N. Yigit, H. Li, E. McDermott, M. Stöger-Pollach, G. Rupprechter, J. Catal. 344 (2016) 1–15.

[45] G.M. Kale, S.S. Pandit, K.T. Jacob, Trans. Japan Inst. Met. 29 (1988) 125–132.

[46] V. V. Atuchin, T.A. Gavrilova, T.I. Grigorieva, N. V. Kuratieva, K.A. Okotrub, N. V. Pervukhina, N. V. Surovtsev, in: J. Cryst. Growth, North-Holland, 2011, pp. 987–990.

[47] G.P. Wirtz, L.B. Sis, J.S. Wheeler, J. Catal. 38 (1975) 196–205.

[48] X. Jing, X. Peng, X. Sun, W. Zhou, W. Wang, S. Wang, Mater. Sci. Semicond. Process. 100 (2019) 262–269.

[49] I. Friberg, N. Sadokhina, L. Olsson, Appl. Catal. B Environ. 250 (2019) 117–131.

[50] T. Lenk, A. Gärtner, K. Stöwe, T. Schwarz, C. Breuer, R. Kiemel, S. Casu, Catalysts 10 (2020) 159.

[51] L.C. Almeida, F.J. Echave, O. Sanz, M.A. Centeno, J.A. Odriozola, M. Montes, in: Stud. Surf. Sci. Catal., Elsevier Inc., 2010, pp. 25–33.

[52] M. Honkanen, M. Kärkkäinen, T. Kolli, O. Heikkinen, V. Viitanen, L. Zeng, H. Jiang, K. Kallinen, M. Huuhtanen, R.L. Keiski, J. Lahtinen, E. Olsson, M. Vippola, Appl. Catal. B Environ. 182 (2016) 439–448.